
Real Time In Vivo Non-invasive Optical Imaging Using Near-infrared Fluorescent Quantum Dots¹

Nicole Y. Morgan, PhD, Sean English, BA, Wei Chen, PhD, Victor Chernomordik, PhD, Angelo Russo, MD, PhD, Paul D. Smith, PhD, and Amir Gandjbakhche, PhD

Rationale and Objective. Deep-tissue optical imaging is of particular interest, as the equipment costs are lower than for competing technologies such as MRI. For this purpose, the development of novel contrast agents with near-infrared (NIR) fluorescence is especially important. We report on the use of NIR semiconductor nanocrystals in deep-tissue in vivo optical imaging.

Materials and Methods. Semiconductor nanocrystals of CdMnTe/Hg were grown in aqueous solution and then coated with bovine serum albumin (BSA). The nanocrystals were approximately 5 nm in diameter and have a broad fluorescence peak in the NIR (770 nm). Nanocrystals were injected either subcutaneously or intravenously into athymic NCR NU/NU and C3H/HENCR MTV mice and then excited with a spatially broad 633 nm source; the resulting fluorescence was captured with a sensitive CCD camera.

Results. We have demonstrated that the nanocrystals are a useful angiographic contrast agent for vessels surrounding and penetrating a murine squamous cell carcinoma in a C3H mouse. Preliminary assessment of the depth of penetration for excitation and emission was done by imaging a beating mouse heart, both through an intact thorax and after a thoracotomy. The temporal resolution associated with imaging the nanocrystals in circulation has been addressed, and the blood clearance for this contrast agent has also been measured.

Conclusions. There was no significant photobleaching or degradation of the nanocrystals after an hour of continuous excitation. The stability of the nanocrystals together with the time resolution of the optical detection makes them particularly attractive candidates for pharmacokinetic imaging studies.

Key Words. Nanocrystals; quantum dots; deep-tissue imaging; near-infrared.

© AUR, 2005

Molecular imaging is a growing field aimed at developing and testing novel tools, reagents, and methods to image specific molecular pathways in vivo, particularly those that are key targets in disease processes. Our current visual assessment of disease is based on anatomic changes

or, in a few specialized cases, physiologic changes that are either a late or indirect manifestation of the molecular changes that underlie a given disease. The ability to image molecular changes will directly affect patient care by allowing earlier detection of disease and identification of specific molecular targets for its treatment. In addition, by directly imaging the underlying alterations of disease, there is the potential to directly image the effects of therapy (1).

In an era when probes are designed to recognize tumor-specific markers and mouse models are designed to exhibit specific cancers, the ability to monitor tumor development from its earliest stages, track metastases, and

Acad Radiol 2005; 12:313–323

¹ From the National Institutes of Health, Bethesda, MD 20892 (N.Y.M., S.E., V.C., A.R., P.D.S., A.G.), and Nomadics, Inc., Stillwater, OK 74074 (W.C.) Received April 1, 2004; revision requested May 17; revision received November 10; revision accepted November 10, 2004. **Address correspondence to:** N.Y.M. e-mail: morgann@mail.nih.gov

© AUR, 2005

doi:10.1016/j.acra.2004.04.023

observe the effects of therapeutics in real time are challenges for molecular imaging modalities. Current techniques for functional imaging include an array of magnetic resonance methods. Blood Oxygen Level-Dependent Magnetic Resonance Imaging (BOLD MRI) (2), or Flow and Oxygenation Dependent Contrast MRI (FLOOD MRI) (3), uses hemoglobin iron as a T_2 relaxation contrast agent to assess oxygen status and/or blood flow changes in a region of tumor tissue. Overhauser-enhanced MRI (OMRI) (4) and Electron Paramagnetic Resonance Imaging (EPRI) (5,6) use the EPR line-width to determine partial pressures of oxygen in tissue. These techniques typically have a spatial resolution of a few hundred microns in the transverse direction, a few millimeters in the axial direction, and a temporal resolution on the order of a minute or more. Alternatively, Positron Emission Tomography (PET) can generate quantitative data concerning the metabolic and hypoxic status of tumor tissue, with a central spatial resolution of 1.8 mm (7–9).

Optical methods for diagnostic and molecular imaging are of particular interest given the relatively low cost as well as the temporal and spatial resolutions associated with such techniques. Visualization of superficial fluorescent events at depths of 350 μm , with an in-plane resolution of 0.5–1.0 μm and a slice thickness of 3–5 μm (10) has been achieved using confocal microscopy. Using two-photon-excited fluorescence microscopy, imaging depths of greater than 600 μm are possible, although this is strongly dependent on the components of the tissue being imaged (11). Furthermore, it is possible to image tissue at depths of 0.5–1.5 mm, with a slice thickness of 15 μm , using infrared (1300 nm) coherence tomography (12). To increase light penetration into tissue it is necessary to employ the near infrared (NIR) spectral range, where most tissue chromophores, including oxyhemoglobin, deoxyhemoglobin, and melanin, absorb comparatively weakly (13). Recently, optical imaging penetration depths on the order of centimeters have been achieved with the use of NIR monochromatic light sources (650–900 nm), together with more sensitive charge coupled device (CCD) cameras.

Different methods for imaging NIR fluorescence have emerged. The most common method, used in this study, is reflectance imaging with continuous wave (CW) irradiation. In this technique, the light source and detector are located on the same side of the region of tissue being imaged. Both excitation and emission radiation are exponentially attenuated as they pass through the tissue. Re-

gions closest to the excitation source are the most strongly illuminated, and light emitted from deep-lying fluorophores will appear both dimmer and more diffuse than that from surface fluorophores (14). However, computational methods are being developed to deconvolve the absorbance and scattering that occurs in deeper regions of tissue (15). More elaborate imaging techniques, such as diffuse optical tomography (DOT) and fluorescence molecular tomography (FMT), use multiple light sources and/or detectors together with computational analysis to generate three-dimensional tomographic images (1).

Over the past twenty years, organic chemists have developed a wide array of molecular probes for a variety of applications in cellular imaging, bio-molecular analysis, sensing, and biophysics. Although the majority of NIR imaging up to now has used organic fluorochromes, the current selection of NIR organic dyes leaves much to be desired. Broad spectral overlap, photobleaching, difficult conjugation chemistry, poor water solubility, and expense are frequently cited as limitations of commercially available organic and metal ion chelate probes. The photo-physical behavior of semiconductor nanoparticles may offer a promising way to solve some of these problems (16–18). The size of these nanocrystals, also known as quantum dots, is comparable to the exciton Bohr diameter; as a result, the energy gap of the nanocrystals is larger than that of the bulk semiconductor due to quantum confinement, and the optical properties of the nanocrystals are strongly size-dependent (19). Slight variations in the chemical synthesis can be used to control the size and composition of the semiconductor core, and so to tailor the spectral characteristics of the nanoparticles. Surface modification techniques can then be used to add biological function and to minimize non-specific interactions without significantly affecting the optical properties. More importantly, as long as the semiconductor core is well-encapsulated, the specific photochemical reactions that cause organic dyes to photobleach are not a problem for inorganic nanoparticles. An additional advantage is the large separation between the excitation and emission wavelengths, which enables more efficient filtering of the excitation source and permits multiwavelength imaging with a single excitation source.

Nanoparticles have been used as luminescent probes for optical imaging (16,17,20–33), and as magnetic probes for NMR imaging (34). The use of near-infrared luminescent nanoparticles (35,36) is being explored. Two recent studies showed the potential of core-shell nanocrystals in noninvasive imaging, one focusing on sentinel

lymph node mapping (37), and the other investigating different surface coatings (38). Here, we report *in vivo* imaging using a CdMnTe/Hg NIR nanoparticle contrast agent coated with BSA, and demonstrate the use of these nanoparticles as an angiographic contrast agent for vessels surrounding and penetrating a murine squamous cell carcinoma in a C3H mouse. Additionally, we have taken preliminary steps to assess the depth of penetration for excitation and emission by imaging a beating mouse heart, both through an intact thorax and after a thoracotomy. The temporal resolution associated with imaging the nanoparticle in circulation has been addressed, and the blood clearance for this contrast agent in the same C3H mouse has also been measured. Control experiments showed minimal decrease in the fluorescence of the nanoparticles, due to photobleaching or degradation, over an hour of continuous illumination, in strong contrast to ICG, a popular NIR molecular dye. There was no apparent toxicity associated with administration of this nanocrystal over the course of the imaging experiments or for a similar dose administered via subcutaneous injection and monitored over a three-day period.

MATERIALS AND METHODS

Nanocrystal Synthesis and Preparation

CdMnTe nanocrystals were used because of the potential applications for combined electron paramagnetic resonance (EPR) and fluorescence imaging. Mn^{2+} has strong EPR signals (39), but Mn^{2+} doping does not affect the absorption edge or reduce the fluorescence of the nanocrystals. The CdMnTe nanoparticles used in this study were prepared by rapidly mixing precursors containing cadmium perchlorate hydrate and hydrogen telluride (H_2Te), using minor modifications of a wet chemical technique widely used for making CdTe nanoparticles (40). Cadmium perchlorate hydrate (Aldrich, Milwaukee, WI), manganese nitrate (99.9%, Alfa Aesar, Ward Hill, MA), aluminum telluride (99.5% pure, CERAC, Milwaukee, WI), and thioglycolic (mercaptoacetic) acid (Aldrich) were used as received. H_2Te gas was obtained from the reaction of excessive amounts of Al_2Te_3 and $0.5M H_2SO_4$ in a nitrogen atmosphere. The Cd^{2+} containing solution was prepared as follows: 0.658 g of $Cd(ClO_4)_2 \cdot H_2O$ and 0.042 g $Mn(NO_3)_2$ were dissolved in 125 mL of water.¹

¹ The ratio of chemical precursors leads to particles with stoichiometry $Cd_{0.95}Mn_{0.05}Te$, the states and distribution of Mn^{2+} in the particles are not clear yet and are under investigation by EPR and element mapping.

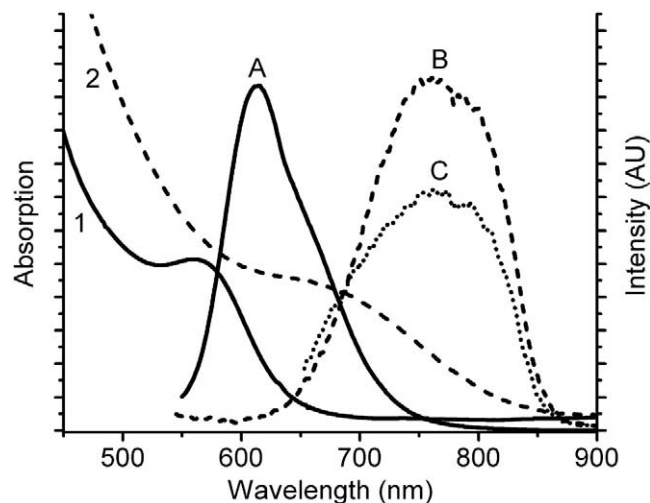


Figure 1. Spectral characteristics of the CdMnTe/Hg/BSA nanocrystals used for this study, as well as uncoated CdMnTe nanocrystals before mercury-doping. The **solid lines** are the absorption spectrum (1) and emission spectrum (A), taken with 450 nm excitation, of the CdMnTe nanocrystals. The **broken lines** are the absorption spectrum (2) of the BSA-coated CdMnTe/Hg nanocrystals used for these experiments, together with emission spectra taken with 525 nm excitation (B) and 633 nm excitation (C). Although the fluorescence is stronger with 525 nm excitation, 633 nm excitation was used for this work because longer wavelength light penetrates further into the tissue. All measurements were performed in aqueous solution.

0.3 mL of thioglycolic acid (TGA) was added and the solution pH was adjusted to ~ 10 with 0.1M NaOH. The solution was then purged with nitrogen for at least 30 minutes prior to introduction of the H_2Te gas.

After the completion of this reaction at room temperature, the solution of CdMnTe nanocrystal nuclei was refluxed at $100^\circ C$ to promote crystal growth. The size of the particles was controlled by the reaction time. Mercury-doping of the CdMnTe nanocrystals was achieved as reported for CdTe/Hg nanoparticles (35,36): 2.5 mL of 0.1 M mercury perchlorate solution was added to 50 mL of CdMnTe nanocrystal solution after synthesis. Finally, the nanocrystals were coated with BSA using EDC (1-(3-dimethylaminopropyl)-3-ethylcarbodiimide hydrochloride, Aldrich) and sulfo-NHS (*N*-hydroxysuccinimide, Pierce Biotechnology Inc., Rockford, IL), coupling agents (41).

Nanocrystal Characterization

Figure 1 displays the absorption and emission spectra of CdMnTe and CdMnTe/Hg-BSA nanoparticle solutions. The BSA coating does not affect the optical properties above 400 nm. The average diameter of the nanoparticles used for this

work, estimated by comparing the absorption spectrum of the CdMnTe nanoparticles with that of CdTe nanoparticles, is approximately 5 nm. The absorption edge shifts from 600 nm to 750 nm as Hg is substituted for Cd into the CdMnTe nanoparticles (35,36). Because the substitution of Cd²⁺ by Hg²⁺ occurs at room temperature, it is assumed that the particle size is unchanged. The emission of the CdMnTe nanoparticles has a peak at 624 nm, arising from the band-band transition of the particles, and a shoulder at 660 nm, which may correspond to the intra-band transition of Mn²⁺ (42). The CdMnTe/Hg-BSA nanoparticles have a broad fluorescent emission, with a peak at approximately 780 nm. Although a shorter-wavelength excitation would more efficiently excite the nanocrystals, 633 nm helium-neon laser excitation was used for the imaging experiments to avoid hemoglobin absorbance and achieve greater tissue penetration. The absorption spectrum shows that a slightly longer wavelength excitation (650–700 nm) would excite the nanocrystals as efficiently, while penetrating somewhat further into the tissue.

Optical Instrumentation

All images were taken with a Princeton Instruments TE-CCD camera (Roper Scientific, Trenton, NJ), using a 50 mm Nikkor lens with an added 3T close-up lens (Nikon, Tokyo, Japan). For the typical focal distance used for this experiment, the in-plane resolution was approximately 60 μm . For the fluorescence images, the subject was illuminated with a helium-neon laser (633 nm) defocused to provide a broad spot at an incident angle of approximately 30 degrees. The excitation power density was measured with a handheld power meter (Coherent, Santa Clara, CA) held normal to the beam; a typical value for this experimental setup is 1.4 mW/cm². All comparative data shown in this paper have been normalized for variations in illumination intensity, typically about 20% between measurements, as well as for optical collection efficiency (aperture size). An interference filter (HQ770/95, HQ790/95, Chroma, Rockingham, VT) was used when collecting fluorescence. The filters have high, uniform transmission within a particular band; the HQ790/95 blocked the laser light more efficiently and was used for later experiments. For control experiments using indocyanine green (ICG) a 780 nm solid-state diode laser was used with a Chroma HQ845/55 interference filter.

For the time dependent data, a time sequence of fluorescent images was first obtained. A small (2–3 mm)

region of interest (ROI) from the area exhibiting peak fluorescence was selected, and the average fluorescent intensity of that ROI plotted as a function of time. For later times, the exposure time was increased to improve the signal-to-noise ratio; the data have been normalized accordingly.

Mice

Female C3H/HENCR MTV and athymic NCR NU/NU mice (NCI, Frederick, MD), were used for experiments in this study. The mice were 6–8 weeks old and weighed 20–30 g at the time of these studies. All experiments were carried out in compliance with the Guide for the Care and Use of Laboratory Animal Resources, (1996) National Research Council, and were approved by the National Cancer Institute Animal Care and Use Committee.

Tumors were grown in C3H mice by administering a subcutaneous injection of 5×10^5 murine squamous cell carcinoma cells to the lateral aspect of the right hind leg. Imaging experiments were performed eight days following inoculation of the tumor cells when the tumor was approximately 10 mm in diameter ($\sim 500 \text{ mm}^3$).

Tail Vein Cannulation

A mouse was first immobilized in a Lucite jig, and while conscious, its tail was cannulated with a catheter consisting of a 30G 1/2 inch needle fixed in one end of a piece of polyethylene tubing (PE 10) and a broken-off 30G 1/2 inch needle in the other end. Each catheter was filled with Heparin Lock flush (100 U/mL) before cannulation, and fixed in place with Vetbond skin adhesive and tape after insertion. Each mouse received 50–100 μl of Heparin IV to maintain flow in the cannula throughout the experiment.

Intubation

Each mouse was anesthetized with an intraperitoneal (IP) injection of a ketamine/xylazine cocktail (ketamine 100 mg/mL, xylazine 20 mg/mL). The neck was slightly hyperextended, the vocal folds and rima glottidis were illuminated, and a 24G 3/4 inch angiocatheter (without stylet) was inserted into the trachea. Isoflurane was aerosolized via medical air at 1%, 300 mL/min, and the mouse was ventilated through the intratracheal tube with a Harvard rodent ventilator, model 683 (Holliston, MA) at 150–160 breaths/min. The ventilation volume was set to generate the same amount of chest rise as was initially observed when the mouse was anesthetized with ketamine/xylazine.

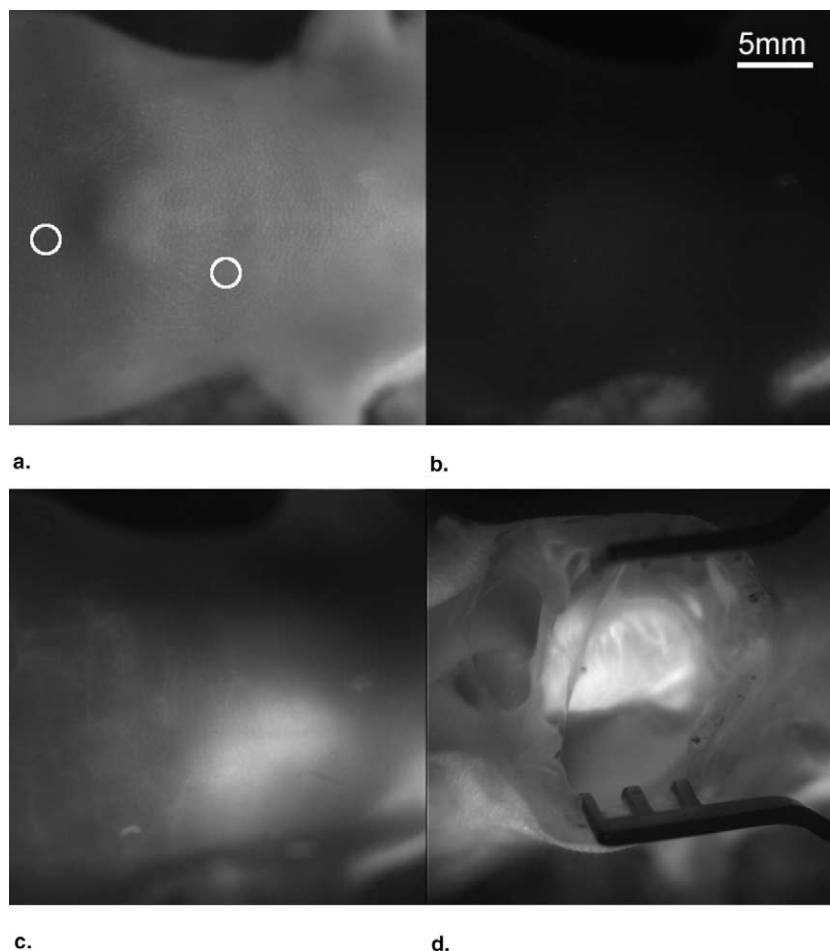


Figure 2. Four pictures of the thoracic and upper abdominal regions of a mouse. The mouse was anesthetized, intubated, and ventilated before these images were taken. **(a)** white-light image of the mouse, with circles indicating the anatomical regions used for the pharmacokinetic data presented in Figure 6. **(b)** the fluorescent background prior to nanocrystal injection, measured with 633 nm excitation and a Chroma HQ 790/95 filter. The light in the lower part of the image is from the felt underneath the animal. **(c)** fluorescence image of the same mouse approximately 17 seconds after a 125 μL jugular bolus of nanocrystals. **(d)** fluorescence image of the same mouse taken 16.5 minutes later, after performing a thoracotomy and approximately 13 seconds after administration of a second 125 μL external jugular bolus of nanocrystals. The same intensity scale has been used for the three fluorescence images.

External Jugular Vein Cannulation

After anesthetizing the mouse with either 220 μl ketamine/xylazine or isoflurane carried by medical air (1.5%, 700 mL/min), an incision was made through the skin and integument over the right or left ventral surface of the neck. Dissection of the cleidomastoideus and sternomastoideus was followed by exposure of the right or left external jugular vein. Fatty tissue was removed and peripheral vessels were cauterized to minimize blood loss. A catheter, like that described previously for tail vein cannulation, was inserted into the jugular vein and fixed in place with Vetbond tissue adhesive. Each mouse received Heparin Lock flush boluses

(50–100 μl , 100 U/mL) to verify and maintain the integrity of the cannula.

Thoracotomy and Heart exposure

After anesthetization and intubation, the skin over the cephalad portion of the abdomen and the thorax was incised with surgical scissors, and the linea alba as well as the pectoralis and the rectus abdominal muscles were exposed and dissected. The thorax was then opened through the sternum and ribs, and intercostal vessels were cauterized to minimize bleeding. The tho-

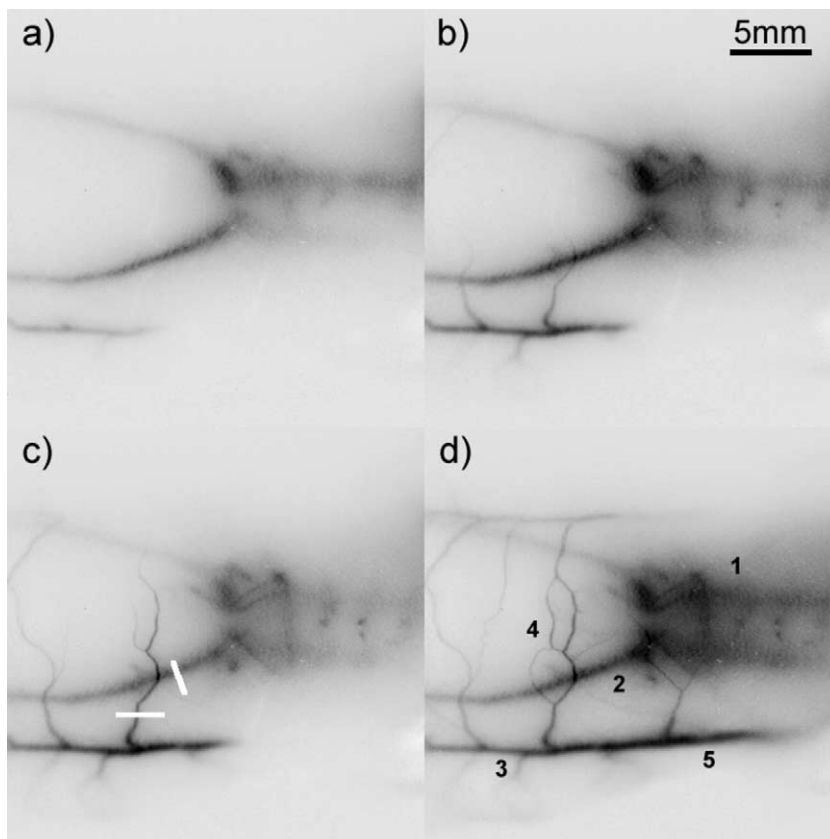


Figure 3. Montage of arterial and venous circulation in the thoracic and abdominal regions of a mouse **a)** 6.8 s, **b)** 9.5 s, **c)** 10.8 s, and **d)** 40.5 s after administration of the nanocrystal bolus. The mouse has been ventilated with a greater than normal air volume, in order to better visualize the vessels, as described in the text. In panel c), white lines indicate cross-sections used for vessel depth analysis performed in Figure 4. The following major vessels are visible and marked in panel d): internal thoracic arteries (1), musculophrenic arteries (2), thoracoepigastric vessels (3), thoracoabdominal vessels (4), and lateral thoracic vessels (5). The background fluorescence, measured before nanocrystal injection, has been subtracted from this sequence and the colormap inverted.

rax was held open with retractors, and the ventilation volume was increased to account for the absent positive end expiratory pressure and to inflate the lungs to near physiologic capacity.

Blood Clearance

For blood collection, tail veins of two different C3H mice were cannulated, and each mouse was anesthetized with 300 μ l ketamine/xylazine. To establish a central line, the neck was dissected and the external jugular vein was exposed and cannulated. The integrity of each line was established with a heparin lock flush bolus (\sim 20 μ l, 8 U/mL). After the two cannulas were inserted in succession, each mouse was given an iv bolus of heparin lock flush (200 μ l, 100 U/mL), via the tail vein cannula, two

minutes before a baseline 10 μ l blood sample was collected. This was done to heparinize the blood and reduce coagulation after a blood sample was taken. A 100 μ l bolus of the nanocrystals (1:1.5 CdMnTe/Hg-BSA, heparin lock flush 100 U/mL) was injected into the tail vein, and over the course of one hour a series of 10 μ l blood samples were collected from the jugular catheter of each mouse and stored in a plate overnight at 4°C. The fluorescence was then measured using the same experimental setup as for the imaging experiments. Two control experiments were performed. In the first, a 1:10 dilution of the CdMnTe/Hg-BSA was prepared in Heparinized blood, and several 10 μ l volumes were measured under constant illumination over a 65 minute period. For comparison, a second control experiment was performed using ICG.

Testing In Vivo Imaging Resolution

The vessels surrounding and traversing an SCC tumor growing in the right hind leg of a C3H mouse were imaged after inducing and maintaining anesthesia with a 220 μl ketamine/xylazine IP injection. The external jugular vein was cannulated as above. A 125 μl bolus of the nanocrystal solution was administered into the jugular vein, and a series of images was collected over the course of an hour. Subsequently, the skin over the surface of the tumor on the lateral aspect of the leg was removed. Another 125 μl bolus of nanocrystals was then administered; after five minutes, a long-exposure, small-aperture image was taken to maximize spatial resolution.

The heart was imaged after first anesthetizing and intubating an athymic NCR mouse. The right external jugular vein was cannulated as above, and a 125 μl bolus of nanocrystals was administered into the jugular vein. A series of fluorescence images was taken with the chest cavity closed. Subsequently, the thorax and pleural cavity were opened to expose the heart, another bolus of nanocrystals was injected, and a series of fluorescence images was acquired.

To further image a murine heart and surrounding vessels, a female, athymic NCR NU/NU mouse was first anesthetized and intubated. Inhalation volumes were increased to hyper-inflate the lungs and thereby accentuate the collateral vessels returning to the heart. After cannulating the right external jugular vein, a 125 μl bolus of the nanocrystals was administered through into the jugular vein, and a series of fluorescence images was taken with the chest cavity closed.

RESULTS

In Vivo Imaging

Heart and collateral vessels.—Figure 2 shows several ventral views of a single intubated mouse under white-light illumination (a) and with fluorescence imaging both before (b) and after (c and d) nanocrystal injection. Frame (c) clearly shows a broad region of fluorescence corresponding to the heart, thereby demonstrating the ability of the nanocrystal contrast agent to excite and observe fluorescence through 1.5–2.0 mm (as determined by computer tomograms) of skin, muscle, and bone. Upon performing a thoracotomy (d), the heart is clearly identified as the source of the fluorescence, and some apparent vasculature, most likely coronary arteries, are imaged. Integration times ranged from 0.25 s to 0.5 s.

The inhalation volume for the mouse depicted in Fig-

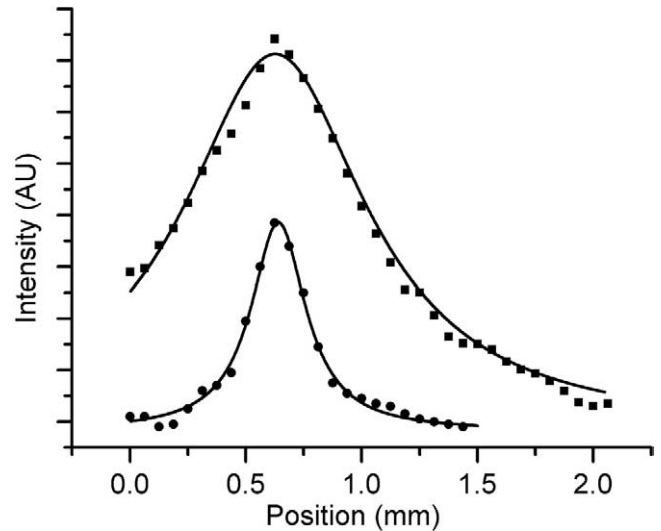


Figure 4. Intensity dependence for the two vessel cross-sections shown in Figure 3c (symbols) together with scattering theory fits to determine approximate vessel depth. For the upper curve (squares), the calculated depth is 340 μm ; for the lower curve (circles), the calculated depth is 90 μm .

ure 3 was increased to hyper-inflate the lungs, thereby accentuating the collateral vessels of the abdomen and thorax returning to the heart. The increased pressure in the lungs results in the compression of capillary vessels and an increased resistance to venous return, which is observed as an increase in the venous volume. The combination of slower blood flow and larger venous volume is most likely what allows better visualization of the venous structure. In addition, the slower circulation is also associated with slower clearance of the nanoparticles from the bloodstream, which could also contribute to the larger fluorescent signals observed.

Figure 3 represents a series of images taken within forty seconds of the nanocrystal injection. The incident illumination was stronger and closer to perpendicular to the animal's skin in the lower part of the image, leading to slightly stronger excitation of the nanocrystals in that region. In the image series, administration of the nanocrystal bolus is observed as it enters the jugular vein. Passage of the bolus to the heart, out through the aorta, and into the subclavian artery is rapid; next, its passage through the internal thoracic arteries and into the musculophrenic and superior epigastric arteries is seen. The musculophrenic arteries are clear, while the superior epigastric arteries are faint. Circulation through the internal thoracic arteries and the perforating branches of the internal thoracic arteries is distinguishable, whereas the perforating arteries provide visualization of the sternal structure, followed by circulation through what appear to be the tho-

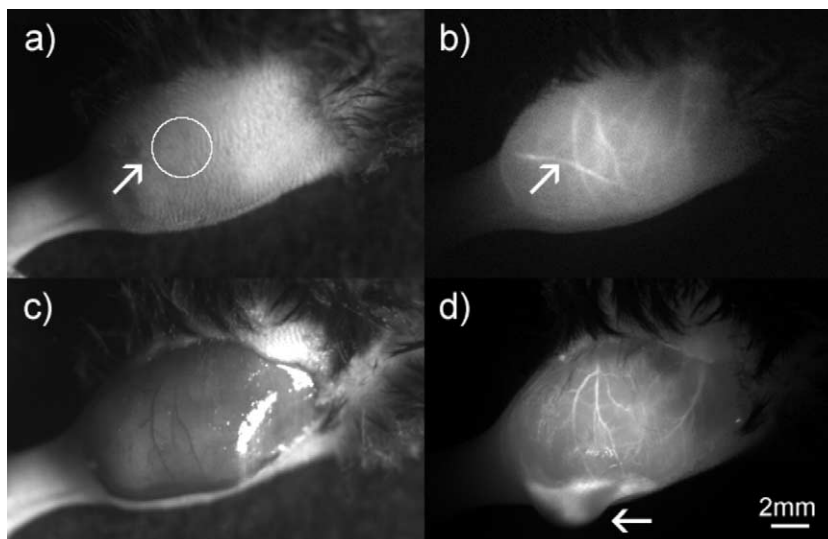


Figure 5. Images of a SCC tumor in the right hind leg of an anesthetized C3H mouse. **(a)** White light image, with a **circle** indicating the area used for the pharmacokinetic data presented in Figure 6. **(b)** Fluorescence image, taken using 633 nm excitation and a Chroma HQ770/95 filter, approximately 130 s after a 125 μ l jugular bolus of nanocrystals. **(c)** White light image of the same tumor after removal of the dermis, with the **(d)** corresponding fluorescence image, using a long exposure time (10 s), taken approximately 18.5 minutes after a second injection of nanocrystals (100 minutes after the first nanocrystal injection, shown in image (b)). The superficial vessels are visible in both the white light and fluorescence images, but the branching of deeper vessels is only seen in the fluorescence image. A number of the major vessels observed with the dermis removed (d) can be seen through the intact dermis (b); however, one major vessel (marked with an **arrow**) apparently running through the dermis is no longer visible in the image (d). The **arrow** in panel (d) marks fluid pooled after dissection of the skin.

racoepigastric, thoracoabdominal, and lateral thoracic veins. However, it is unclear as to why the lateral thoracic arteries were not observed in the early images. One factor is simply that for this experiment the right lateral thoracic artery is further from the light source; in addition, the size of the artery is smaller than the complementary vein.

For accurate quantification of signals coming from structures below the skin surface, the depth of the vessel under investigation is important. In order to estimate the depths of the vessels observed in the abdominal region of the mouse shown in Figure 3, the scattering theory of (15) is applied. Figure 4 shows the fluorescent intensity along the two vessel cross-sections marked with lines shown in Fig. 3c. These data were then fitted using the random-walk scattering theory of (15), assuming that the vessels are 1-D fluorescent sources; the results are shown as solid lines in Fig. 4. The calculated depths associated with these and other curves are 90 μ m to 400 μ m. We note that this preliminary analysis assumes zero vessel width; in reality the observed vessels are perhaps 200 μ m in diameter. However, even this gross approximation shows that the signal collected on the surface should be deconvolved from the scattering by tissue layers.

In Vivo Imaging

Tumor.—The ability to distinguish the superficial vessels associated with an SCC tumor was also demonstrated. In Figure 5, with an in-plane resolution of approximately 120 μ m, a network of blood vessels can be seen in the fluorescence images (b and d). Although at least one of the major vessels (arrow in a, b) is in the skin layer, other vessels seen in (b) are still present after the skin is dissected (d), and had been imaged through the (\sim 1 mm) layer of removed tissue. Considering the white light image of Figure 5a, even the superficial vessel indicated by the arrow is better visualized using the nanocrystal fluorescence, and the deeper vessels are only visible in the fluorescence images. The diffuse brightness is most likely associated with the capillary network of the tumor, and in conjunction with numerical modeling could be used to provide an estimate of tumor blood volume.

Pharmacokinetics

Given the spectral characteristics of the nanocrystals and the sensitivity of the instrumentation, the temporal resolution of this technique makes it well suited for pharmacokinetic

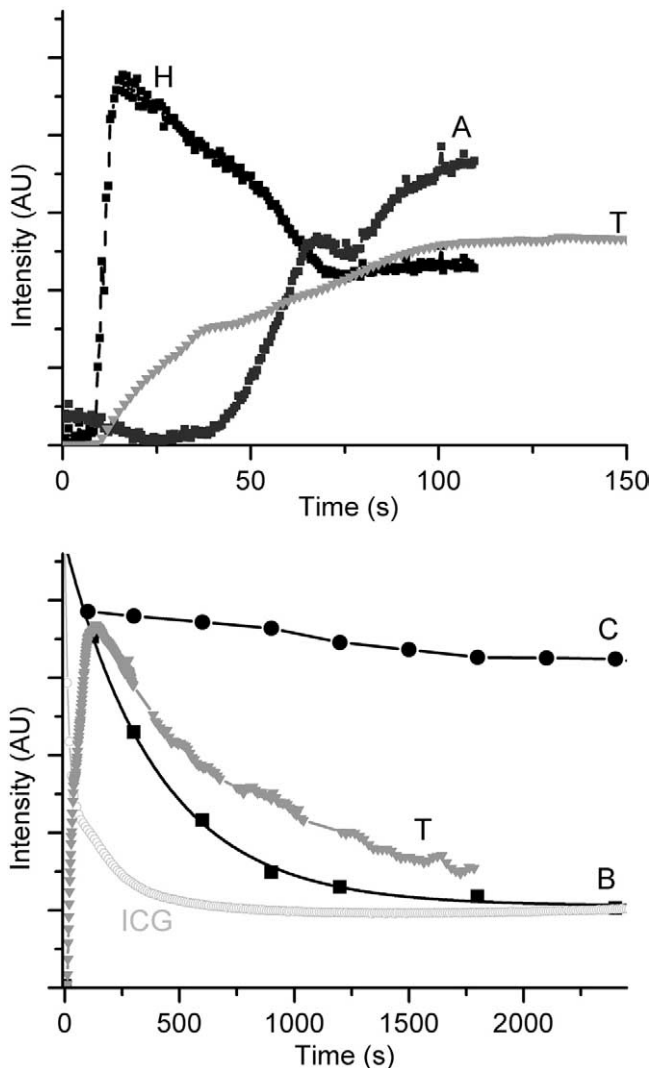


Figure 6. Clearance of nanocrystals from the blood stream, as measured through direct fluorescence imaging of the live animal as well as from fluorescence of blood drawn at regular intervals after nanocrystal injection. The background fluorescence, as measured before nanocrystal injection, has been subtracted. In the **upper panel**, a comparison of the short-time response for three different tissue areas: the heart (H) and abdominal (A) areas from Figure 2, and the tumor (T) tissue of Figure 5. In the **lower panel**, the longer-time clearance measured for the tumor tissue (T) of Figure 5, together with data from periodic blood draws (B) as well as two control measurements (C, ICG) are shown. The tumor data in the lower panel has been adjusted by an arbitrary scaling factor to facilitate comparison of the curve shapes. The blood draw data has been fitted with an exponential form ($A\exp(-x/t) + y_0$, $y_0=52.8$, $A=234$, $t=405$, $R^2=.998$); all other lines are guides to the eye. The ICG and nanocrystal (C) fluorescence are normalized to similar values at short times; the ICG shows a rapid early decrease, barely visible on this scale.

analyses. Figure 6 presents preliminary data on the elimination of the nanocrystals from various tissues, including the blood. These time-dependence series were obtained from

fluorescence images like those shown in Figures 2 and 5 by averaging the fluorescent intensities in small ROIs for each tissue and then plotting the average intensities as a function of time. The data on the heart and abdomen were obtained from the mouse shown in Fig. 2, with the circular ROIs used for the time series marked in Fig. 2a. The region of great intensity observed over and to the left of the sternum, which most likely corresponds to the left ventricle of the heart, was used to generate the nanocrystal elimination curve for the heart plotted in Figure 6. The other circle in Figure 2a was used to generate the abdominal data; as seen in Figure 6, this upper abdominal region exhibited uptake of the nanocrystals over the course of image collection and likely represents the liver. The data on the tumor tissue was obtained from the mouse shown in Figure 5. In each case, the background fluorescence, as measured before injection of the nanocrystals, has been subtracted.

For the blood data, blood samples were drawn from two different mice at regular intervals after nanocrystal injection. These blood samples were then placed in wells and measured using the same experimental setup as for the in vivo imaging experiments. The blood data in Figure 6 represents the average intensity for the two mice at each time point. The fluorescence of another blood sample, of similar volume without nanocrystals added, has been subtracted from the raw signal intensity. The representative tumor and blood curves have also been adjusted by arbitrary scaling factors in order to compare the shapes of the elimination curves for the different tissues.

To determine if any component of the decay in the nanocrystal fluorescence within the different tissues was due to photobleaching or degradation of the nanocrystals, the fluorescence of a blood-nanocrystal mixture was measured over the course of an hour under continuous excitation. The results are plotted as circles in Fig. 6b; as was done for the other blood samples, the fluorescence of a similar volume of blood without nanocrystals has been subtracted. While there is a slight decrease in fluorescence with time, the changes we observe in the imaging and blood draws are clearly dominated by elimination of the nanocrystals from the blood rather than a decrease in the nanocrystal fluorescence. The blood phantom data demonstrate that these CdMnTeHg/BSA nanocrystals are reasonably stable under physiological conditions, and in particular do not photobleach like conventional fluorescent dyes. In contrast, similar measurements on phantoms of indocyanine green (ICG), a commonly-used NIR dye, show pronounced photobleaching over an hour of continuous excitation. The difference in photobleaching is extremely important for pharmacokinetic studies: whereas the

elimination or uptake of the nanocrystals could be directly measured by changes in fluorescent intensity, extracting parameters for the trafficking of an ICG-tagged probe would require modelling the cumulative light exposure of the dye as it passes through different parts of the tissue.

Considering the *in vivo* elimination curves in Figure 6, the high speed image collection allows for better tracking of the short-time uptake and redistribution of the nanocrystals than could be achieved through blood draws. Furthermore, the stability of the nanocrystals permits good overlap between the imaging data and the blood sample data; the combination of the two techniques should permit the measurement of pharmacological data over a large range of times. The data obtained from blood samples has been fitted with an exponential form, plotted in Fig. 6, from which a decay time of approximately 400 s was determined. The apparent steady-state value of the fluorescence could correspond to another, much slower decay with a time constant in days.

For the tumor tissue, both uptake and elimination of the nanocrystals are observed. The relatively slow elimination observed for the tumor tissue, when compared to the measurements of the blood draws, suggests that exchange of the nanocrystals between the circulation and the tumor tissue may be different and/or compromised (43). Although suggestive, further experiments are needed—the mouse with the implanted tumor is of a different type (C3H) from that used for the heart and liver elimination/uptake curves (NCR).

CONCLUSIONS

We have demonstrated the ability to use the CdTeMnHg-BSA nanocrystals as a fluorescent, angiographic contrast agent in the NIR range. Blood vessels on the order of ~ 100 μm in diameter, located at a depth of several hundred microns have been visualized, and a beating heart has been imaged through 1–2 mm of skin, fat, and bone. We observed no significant photobleaching or degradation of the nanocrystals over the time scale of any of the phantom or *in vivo* experiments (hours). Other experiments (not shown) using ICG as a contrast agent gave similar visualization of embedded sources; however, ICG phantoms show substantial photobleaching, which suggests that nanocrystals are superior for quantitative real-time monitoring. Nonetheless, there are still issues that need to be addressed before nanocrystal probes can be broadly used in biomedical applications. In particular, the long-term biocompatibility of inorganic nanoparticles needs to be improved, and the potential toxicity of

the nanoparticles needs to be investigated further. These limitations may be overcome by refining the surface coatings or encapsulation of the nanoparticles. BSA was used as a coating agent for these nanocrystals; however, over time (weeks), some precipitation was observed in the stock solution. Silica is chemically and biologically inert, and the use of a silica coating has already been demonstrated as an effective means of improving nanoparticle solubility and biocompatibility (16). More recently, liposomes of n-polyethylene glycol (PEG) phosphatidylethanolamine (PE) have been used as a nanocrystal coating, and the encapsulation of CdSe/ZnS nanocrystals with PEG-PE has been used to observe *Xenopus* embryonic development *in vivo* (31). A recent study of nanocrystal cytotoxicity in cultured hepatocytes further emphasized the importance of robust encapsulation in preventing Cd²⁺ ion release and cell death (44).

With preliminary experiments and analyses, we have shown the ability to study the pharmacokinetics associated with CdTeMnHg/BSA nanocrystals. More extensive studies could be performed to characterize the elimination of this nanocrystal in this or other animal models. Along with gaining an understanding of the pharmacology of this agent we would like to target this and other nanocrystals to specific tissues. The use of proper shell functional groups as well as proper cross-linking agents and the establishment of non-covalent bonding, such as electrostatic interactions with other agents, could aid in nanocrystal trafficking.

NIR nanocrystals offer substantial advantages over conventional fluorophores for deep-tissue biomedical imaging. In particular, the strong luminescence and the resistance to photobleaching make them ideal candidates for pharmacokinetic studies. Although issues of toxicity need to be addressed, substantial progress can be made in animal studies with currently available nanocrystals. Furthermore, advances in handling and tagging these materials should be directly transferable if new types of nanocrystals, made with less-toxic materials, become available in the future.

ACKNOWLEDGMENTS

Wei Chen would like to thank NIH (Grant Nos. 1R43CA112756-01 and 1R43CA110091-01), the US Army Medical Research and Materiel Command (Contract No. W81XWH-05-C-0101), and Nomadics, Inc. for financial support.

REFERENCES

1. Weissleder R, Mahmood U. Molecular imaging. *Radiology* 2001; 219:316–333.

2. Ogawa S, Lee TM, Kay AR, Tank DW. Brain Magnetic-Resonance-Imaging with Contrast Dependent on Blood Oxygenation. Proceedings of the National Academy of Sciences of the United States of America 1990; 87:9868–9872.
3. Howe FA, Robinson SP, Rodrigues LM, Griffiths JR. Flow and oxygenation dependent (flow) contrast MR imaging to monitor the response of rat tumors to carbogen breathing. Magnetic Resonance Imaging 1999; 17:1307–1318.
4. Krishna MC, English S, Yamada K, et al. Overhauser enhanced magnetic resonance imaging for tumor oximetry: Coregistration of tumor anatomy and tissue oxygen concentration. Proceedings of the National Academy of Sciences of the United States of America 2002; 99:2216–2221.
5. Ilangovan G, Li HQ, Zweier JL, Krishna MC, Mitchell JB, Kuppusamy P. In vivo measurement of regional oxygenation and Imaging of redox status in RIF-1 murine tumor: Effect of carbogen-breathing. Magnetic Resonance in Medicine 2002; 48:723–730.
6. Subramanian S, Devasahayam N, Murugesan R, et al. Single-point (constant-time) imaging in radiofrequency Fourier transform electron paramagnetic resonance. Magnetic Resonance in Medicine 2002; 48: 370–379.
7. Kaarstad K, Bender D, Bentzen L, Munk OL, Keiding S. Metabolic fate of F-18-FDG in mice bearing either SCCVII squamous cell carcinoma or C3H mammary carcinoma. Journal of Nuclear Medicine 2002; 43: 940–947.
8. Zhuang HM, Pourdehnad M, Lambright ES, et al. Dual time point F-18-FDG PET imaging for differentiating malignant from inflammatory processes. Journal of Nuclear Medicine 2001; 42:1412–1417.
9. Seidel J, Vaquero JJ, Pascau J, Desco M, Johnson CA, Green MV. Features of the NIH atlas small animal PET scanner and its use with a coaxial small animal volume CT scanner. Proceedings, IEEE International Symposium on Biomedical Imaging. 2002:545–548.
10. Rajadhyaksha M, Gonzalez S, Zavislan JM, Anderson RR, Webb RH. In vivo confocal scanning laser microscopy of human skin II: Advances in instrumentation and comparison with histology. Journal of Investigative Dermatology 1999; 113:293–303.
11. Helmchen F, Denk W. New developments in multiphoton microscopy. Current Opinion in Neurobiology 2002; 12:593–601.
12. Welzel J. Optical coherence tomography in dermatology: a review. Skin Research and Technology 2001; 7:1–9.
13. Ntziachristos V, Bremer C, Weissleder R. Fluorescence imaging with near-infrared light: new technological advances that enable in vivo molecular imaging. European Radiology 2003; 13:195–208.
14. Sevick-Muraca EM, Houston JP, Gurfinkel M. Fluorescence-enhanced, near infrared diagnostic imaging with contrast agents. Current Opinion in Chemical Biology 2002; 6:642–650.
15. Eidsath A, Chernomordik V, Gandjbakche A, Smith P, Russo A. Three-dimensional localization of fluorescent masses deeply embedded in tissue. Physics in Medicine and Biology 2002; 47:4079–4092.
16. Bruchez M, Moronne M, Gin P, Weiss S, Alivisatos AP. Semiconductor nanocrystals as fluorescent biological labels. Science 1998; 281:2013–2016.
17. Chan WCW, Nie SM. Quantum dot bioconjugates for ultrasensitive nonisotopic detection. Science 1998; 281:2016–2018.
18. Chen W, Joly AG, Wang S. Luminescence of Semiconductor Nanoparticles. In: Nalwa HS, ed. Encyclopedia of Nanoscience and Nanotechnology. Stevenson Ranch, CA: American Scientific Publishers, 2003.
19. Chen W. Fluorescence, thermoluminescence, and photostimulated luminescence of nanoparticles. In: Nalwa HS, ed. Handbook of Nanostructured Materials and Nanotechnology. San Diego: Academic Press, 2000; 325–392.
20. Alivisatos AP. Semiconductor clusters, nanocrystals, and quantum dots. Science 1996; 271:933–937.
21. Mitchell GP, Mirkin CA, Letsinger RL. Programmed assembly of DNA functionalized quantum dots. Journal of the American Chemical Society 1999; 121:8122–8123.
22. Mattoussi H, Mauro JM, Goldman ER, et al. Self-assembly of CdSe-ZnS quantum dot bioconjugates using an engineered recombinant protein. Journal of the American Chemical Society 2000; 122:12142–12150.
23. Mahtab R, Harden HH, Murphy CJ. Temperature- and salt-dependent binding of long DNA to protein-sized quantum dots: Thermodynamics of “inorganic protein”-DNA interactions. Journal of the American Chemical Society 2000; 122:14–17.
24. Sun BQ, Xie WZ, Yi GS, Chen DP, Zhou YX, Cheng J. Microminiaturized immunoassays using quantum dots as fluorescent label by laser confocal scanning fluorescence detection. Journal of Immunological Methods 2001; 249:85–89.
25. Pathak S, Choi SK, Arnheim N, Thompson ME. Hydroxylated quantum dots as luminescent probes for in situ hybridization. Journal of the American Chemical Society 2001; 123:4103–4104.
26. Han MY, Gao XH, Su JZ, Nie S. Quantum-dot-tagged microbeads for multiplexed optical coding of biomolecules. Nature Biotechnology 2001; 19:631–635.
27. Klarreich E. Biologists join the dots. Nature 2001; 413:450–452.
28. Mitchell P. Turning the spotlight on cellular imaging—Advances in imaging are enabling researchers to track more accurately the localization of macromolecules in cells. Nature Biotechnology 2001; 19:1013–1017.
29. Niemeyer CM. Nanoparticles, proteins, and nucleic acids: Biotechnology meets materials science. Angewandte Chemie-International Edition 2001; 40:4128–4158.
30. Chan WCW, Maxwell DJ, Gao XH, Bailey RE, Han MY, Nie SM. Luminescent quantum dots for multiplexed biological detection and imaging. Current Opinion in Biotechnology 2002; 13:40–46.
31. Dubertret B, Skourides P, Norris DJ, Noireaux V, Brivanlou AH, Libchaber A. In vivo imaging of quantum dots encapsulated in phospholipid micelles. Science 2002; 298:1759–1762.
32. Michalet X, Pinaud F, Lacoste TD, et al. Properties of fluorescent semiconductor nanocrystals and their application to biological labeling. Single Molecules 2001; 2:261–276.
33. Akerman ME, Chan WCW, Laakkonen P, Bhatia SN, Ruoslahti E. Nanocrystal targeting in vivo. Proceedings of the National Academy of Sciences of the United States of America 2002; 99:12617–12621.
34. Zhang Y, Kohler N, Zhang MQ. Surface modification of superparamagnetic magnetite nanoparticles and their intracellular uptake. Biomaterials 2002; 23:1553–1561.
35. Kershaw SV, Burt M, Harrison M, Rogach A, Weller H, Eychmuller A. Colloidal CdTe/HgTe quantum dots with high photoluminescence quantum efficiency at room temperature. Applied Physics Letters 1999; 75:1694–1696.
36. Harrison MT, Kershaw SV, Burt MG, Eychmuller A, Weller H, Rogach AL. Wet chemical synthesis and spectroscopic study of CdHgTe nanocrystals with strong near-infrared luminescence. Materials Science and Engineering B-Solid State Materials for Advanced Technology 2000; 69:355–360.
37. Kim S, Lim YT, Soltesz EG, et al. Near-infrared fluorescent type II quantum dots for sentinel lymph node mapping. Nature Biotechnology 2004; 22:93–97.
38. Ballou B, Lagerholm BC, Ernst LA, Bruchez MP, Waggoner AS. Noninvasive imaging of quantum dots in mice. Bioconjug Chem 2004; 15: 79–86.
39. Chen W, Sammynaiken R, Huang YN, et al. Crystal field, phonon coupling and emission shift of Mn²⁺ in ZnS : Mn nanoparticles. Journal of Applied Physics 2001; 89:1120–1129.
40. Gaponik N, Talapin DV, Rogach AL, et al. Thiol-capping of CdTe nanocrystals: An alternative to organometallic synthetic routes. Journal of Physical Chemistry B 2002; 106:7177–7185.
41. Wang S, Mamedova N, Kotov NA, Chen W, Studer J. Antigen/Antibody Immunocomplex from CdTe Nanoparticle Bioconjugates. Nanoletters 2002; 2:817–822.
42. Yu YM, Byungsung O, Yoon MY, Kim JB, Choi YD. Effect of Mn concentration on photoluminescence characteristics of Zn1-xMnxTe epilayers. Thin Solid Films 2003; 426:265–270.
43. Brown JM, Giaccia AJ. The unique physiology of solid tumors: opportunities (and problems) for cancer therapy. Cancer Res 1998; 58:1408–1416.
44. Derfus AM, Chan WCW, Bhatia SN. Probing the cytotoxicity of semiconductor quantum dots. Nano Letters 2004; 4:11–18.